



# High-speed polarization-resolved coherent Raman scattering imaging

Matthias Hofer, Naveen K. Balla, Sophie Brasselet

## ► To cite this version:

Matthias Hofer, Naveen K. Balla, Sophie Brasselet. High-speed polarization-resolved coherent Raman scattering imaging. *Optica*, 2017, 4 (7), 10.1364/OPTICA.4.000795 . hal-01643484

**HAL Id: hal-01643484**

**<https://hal.science/hal-01643484>**

Submitted on 13 Apr 2018

**HAL** is a multi-disciplinary open access archive for the deposit and dissemination of scientific research documents, whether they are published or not. The documents may come from teaching and research institutions in France or abroad, or from public or private research centers.

L'archive ouverte pluridisciplinaire **HAL**, est destinée au dépôt et à la diffusion de documents scientifiques de niveau recherche, publiés ou non, émanant des établissements d'enseignement et de recherche français ou étrangers, des laboratoires publics ou privés.

# High-speed polarization-resolved coherent Raman scattering imaging

MATTHIAS HOFER,<sup>†</sup> NAVEEN K. BALLA,<sup>†</sup> AND SOPHIE BRASSELET<sup>\*</sup>

Aix Marseille Univ, CNRS, Centrale Marseille, Institut Fresnel, F-13013 Marseille, France

<sup>\*</sup>Corresponding author: [sophie.brasselet@fresnel.fr](mailto:sophie.brasselet@fresnel.fr)

Received 10 February 2017; revised 7 June 2017; accepted 7 June 2017 (Doc. ID 286295); published 13 July 2017

Polarization-resolved coherent Raman scattering (polar-CRS) provides rich information on molecular orientational organization, with the strong advantages of being a label-free and chemically specific imaging method. Its implementation, however, strongly reduces the imaging acquisition rate, due to limits imposed by polarization tuning. Here we demonstrate fast-polar-CRS imaging based on combined electro-optic polarization and acousto-optic amplitude modulations, applicable to both stimulated Raman scattering and coherent anti-Stokes Raman scattering imaging. The proposed scheme adds polarization information without compromising the capacities of regular CRS intensity imaging; increases the speed of orientational imaging by two orders of magnitude as compared with previous approaches; and does not require post-processing analyses. We show that this method permits sub-second time-scale imaging of lipid order packing and local lipid membrane deformations in artificial lipid multilayers, but also in red blood cell ghosts, demonstrating its high sensitivity down to a single lipid bilayer membrane. © 2017 Optical Society of America

**OCIS codes:** (180.4315) Nonlinear microscopy; (190.2640) Stimulated scattering, modulation, etc.; (260.5430) Polarization; (290.5910) Scattering, stimulated Raman.

<https://doi.org/10.1364/OPTICA.4.000795>

## 1. INTRODUCTION

Coherent Raman scattering (CRS) imaging has progressed considerably over the past decade, making coherent anti-Stokes Raman scattering (CARS) and stimulated Raman scattering (SRS) powerful tools to monitor the presence of specific molecules in cells and tissues [1–4] with real-time imaging capabilities [5,6]. A large amount of work has been dedicated to access of vibrational spectral information at fast time rates, allowing differentiation of species in biological samples at sub-second time scales [7–9].

More recently, increasing effort has been brought to quantify the degree of orientational organization of chemical species using the sensitivity of CRS to polarization [10]. CARS and SRS rely on the illumination of a sample by two synchronized lasers at the Stokes ( $\omega_s$ ) and pump ( $\omega_p$ ) frequencies. CARS results from a nonlinear induced anti-Stokes radiation (frequency  $\omega_{as}$ ), which is enhanced at the resonance condition  $\omega_p - \omega_s = \Omega_r$  [Fig. 1(a)], whereas SRS is quantified by the amount of energy transfer from the pump to the Stokes when both beams are in resonance with a molecular vibration frequency  $\Omega_r$  [4] [Fig. 1(b)]. In both processes, the resulting signal is strongly sensitive to the incident polarizations when the probed vibration bonds are oriented, making it an interesting probe for the degree of molecular orientation inside a focal spot of typically 400 nm size. Initially introduced in CARS imaging, polarization-resolved CRS relies on the monitoring of the CARS signal response to the rotation of the incident

light polarization (either the pump or both pump and Stokes) or the sample itself. Provided that molecular bonds are oriented, this results in a modulation of the detected intensity at  $\omega_{as}$ , which is maximized when the incident polarizations lie along the averaged direction of the bonds' distribution [Fig. 1(c)]. Using such methods, high molecular organization has been evidenced in water molecules between phospholipid layers [11], CN bonds of liquid crystals [12,13], CH bonds of polyglucan chains in cellulose [14], and in various symmetry modes of zeolite crystals [15]. Monitoring the CH<sub>2</sub> vibrational stretching bond in lipids has shown considerable level of information on lipid order within artificial multilayers [16,17], where the measured modulation was used to retrieve quantitative information on sub-diffraction molecular orientational order behaviors, in particular, its mean orientation and angular distribution shape [17]. Lipid order imaging by polarization-resolved CARS has also been applied in myelin, which forms dense lipid multilayers around axons. Myelin structural imaging has been demonstrated in fixed tissues in mouse brain [18,19] and sciatic nerve [20], as well as in the spinal cord of mice [17,21] and anesthetized zebrafish [22]. Being able to monitor lipid order without the need of fluorescent labels ultimately brings new knowledge on lipid packing properties, which is critical for the structural integrity of myelin in the central and peripheral nervous systems, with consequences in neuropathologies [20–22]. More generally, lipid packing plays a role in the maintenance of skin lipid barriers, in cell signaling, and in cell

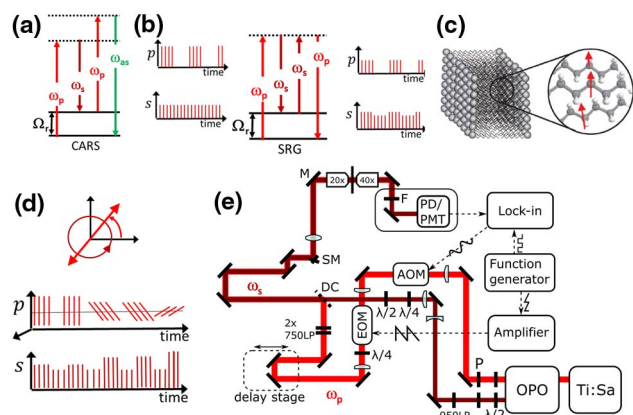


**Fig. 1.** (a) Principle of CARS, depicting the pump ( $\omega_p$ ), Stokes ( $\omega_s$ ), and anti-Stokes radiation ( $\omega_{as}$ ) frequencies, as well as the resonant vibration ( $\Omega_r$ ). (b) Principle of SRS (here SRG). The schematics show the time sequences of the modulated incident pump and monitored Stokes, which are both affected by the resonance. (c) Schematic representation of a lipid bilayer with nonlinear induced dipoles (red arrows) lying along the CH bonds probed at  $2845\text{ cm}^{-1}$ . (d) The pump (linear rotating) and Stokes (circular) are represented in the sample plane as well as the resulting double modulation produced for the Stokes beam when the pump is modulated in polarization and intensity. (e) Optical setup. M, mirror; SM, scanning mirrors; DC, dichroic mirror; PD, photodiode; PMT, photomultiplier; AOM, acousto-optic modulator; EOM, electro-optic modulator (Pockels cell); OPO, optical parametric oscillator.

mechanics. Recently, polarization-resolved CARS has been extended to SRS, emphasizing the major advantage of avoiding correction for the non-resonant background polarization dependence, which tends to underestimate molecular order in conditions of low signal to noise [23].

Obtaining orientational information from polarization-resolved CRS allows access to molecular-scale processes that are not visible in pure intensity images. Yet currently developed techniques are not able to address fast time scale dynamics, the main reason being the requirement of point scanning modalities. Typical molecular order imaging is performed at the rate of minutes for sequential polarization tuning on images of  $150 \times 150$  pixels [17,19,21,22], to tens of seconds in schemes using synchronization between line scanning and polarization rotation [20]. This limits the current applicability to minute-scale processes, with the obvious inconvenience of sensitivity to sample motion and lack of dynamics information.

CRS microscopy is nevertheless potentially able to reach much faster acquisition rates, as expected from its intrinsic noise limits [9]. In all polarization-dependent CRS methods, the polarization is varied in steps but not modulated continuously, preventing faster lock-in-based methods to be implemented. Only a few examples of fast-polarization modulation have been reported, based on modulation of polarization between two perpendicular states only [24], which leads to faster rates but loses the full information (orientation and shape) on the molecular distribution [10]. Electro-optical modulation of polarization at a rate of a few kHz has been used in second-harmonic generation (SHG), the SHG modulation phase being detected by lock-in amplification in regions of oriented molecules [25], or in homodyne SHG by interference with a reference SHG beam [26]. However, these schemes did not extract molecular order information.

We propose here a method that exploits the benefit of high-speed electro-optical polarization modulation of the pump beam (in principle up to MHz as limited by electronics bandwidth) and lock-in amplification, to read-out molecular order and orientation at a fast rate, e.g., exploiting both amplitude and phase information. In polarization-resolved SRS, this approach uses Stokes beam modulation as a result of energy transfer from the pump beam; however, in contrast to traditional SRS, the energy transfer occurs only in regions of the sample where molecules are aligned. Polarization modulation is thus a new source of stimulated Raman gain (SRG) or loss, sensitive to not only vibrational specificity, but also orientational behavior. Additionally, we show that such polarization modulation can be combined with intensity monitoring in a double modulation mode to retrieve not only a molecular bond density map, but also an absolute value of molecular order per pixel (e.g., the width of angular distribution explored by molecular bonds in the focal volume). We finally show that, similarly to SRS, this scheme is also applicable to polarization-resolved CARS, with fast dynamics and high sensitivity down to single lipid bilayer in cells.

## 2. PRINCIPLE OF FAST-POLARIZATION CRS IMAGING

In regular SRS, here used in the SRG mode, the power gain in the Stokes beam is measured at the modulation frequency of the pump beam, which acts as a local oscillator. In a medium where molecular bonds are oriented, a rotation of the pump linear polarization will induce a modulation of the signal, due to variation of the energy transfer efficiency from high (molecular bonds parallel to pump polarization) to low (molecules bonds perpendicular to pump polarization) [Fig. 1(d)]. The sinusoidal variation of the SRG signal carries, in particular, information of the degree of orientational order of molecular bonds (amplitude of the signal modulation) and its average direction (phase of the modulation). Accessing these two quantities simultaneously is essential to addressing both the molecular-scale behavior of orientational disorder (within the diffraction limit size of about  $400\text{ nm}$ ) and its orientation over larger mesoscopic scales (within the distance of a pixel, typically  $100\text{ nm}$ – $300\text{ nm}$  size) (see Supplement 1) [23].

Fast-polarization modulation aims at measuring these amplitude and phase parameters simultaneously, using a fast rotation of the pump linear polarization direction, while the Stokes polarization remains circular to avoid artificial photoselection from this beam [Fig. 1(d)]. This scheme is imposed by the chromatic nature fast-polarization modulators. In the present method, the incident pump and Stokes wavelengths come from a  $180\text{ fs}$ – $80\text{ MHz}$  Ti:sapphire laser followed by an optical parametric oscillator, set at, respectively,  $781\text{ nm}$  and  $1004\text{ nm}$ , in resonance with the vibration frequency of  $2845\text{ cm}^{-1}$  of the  $\text{CH}_2$  symmetric stretching vibration mode active in lipids [Fig. 1(d)]. The optical resolution of the optical setup used for coherent nonlinear third-order processes is about  $437\text{ nm}$  lateral and  $1.6\text{ }\mu\text{m}$  axial (see Supplement 1). The pump beam is amplitude-modulated by an acousto-optic modulator (AOM) at a typical frequency of  $2\text{ MHz}$ , and further polarization-modulated by an electro-optic modulator (EOM) at a  $100\text{ kHz}$  frequency followed by a quarter-wave plate [Fig. 1(e); see Supplement 1, Fig. S1]. Note that the EOM modulation frequency used here is only limited by the



bandwidth of the amplifier. To provoke a sinusoidal SRS or CARS modulation due to polarization, the EOM is driven by a periodic voltage ramp that provides a regular sweep of the in-plane linear polarization angle  $\alpha$  in the range of  $[0^\circ\text{--}180^\circ]$  (see Supplement 1, Fig. S2). The measured signal from the photodetector is split into two independent input channels of the lock-in. A homodyne lock-in detection is applied by using the reference signals that modulate the AOM (internally generated by the lock-in) and EOM (generated by the function generator). Both channels are simultaneously demodulated at their respective modulation frequencies, retrieving the amplitude of the AOM modulation on one side and the amplitude and phase of the EOM modulation on the other side. The quality of the rotating linear polarization produced is seen to be high with negligible ellipticity and a slight residual di-attenuation (see Supplement 1, Figs. S2 and S3).

For both SRS and CARS modalities, the polarization modulation leads to a  $\alpha$ -dependent modulated response of the signal of the form (see Supplement 1)

$$I^{\text{SRS,CARS}}(\alpha) \propto a_0 + S_2 \cos 2(\alpha - \varphi_2), \quad (1)$$

where  $\alpha$  is the rotating pump polarization direction in the sample plane,  $a_0$  is the total measured intensity, and  $S_2$  and  $\varphi_2$  represent, respectively, the amplitude and phase of the second-order induced modulation. Here we do not represent higher harmonics that could be treated as additional information [17].  $S_2$  and  $\varphi_2$  are, respectively, related to the degree of alignment of molecular bonds within the focal spot of the microscope objective and to its average orientation (see Supplement 1). In particular,  $S_2$  is equal to 0 in isotropic samples, and increases with increasing order, e.g., decreasing width of the molecular angular distribution excited in the focal volume. Note that the relation between the obtained  $(S_2, \varphi_2)$  parameters and the intrinsic molecular order taking place within the focal spot of the microscope can be directly related to regular polarization-resolved CARS and SRS [17]. In particular, it can be shown that when the polarization dependence of the measured intensity is truncated to its second-order Fourier series such as done in Eq. (1), the tensorial components combinations of the macroscopic third-order nonlinear tensor that are probed in both CARS and SRS processes are identical when they are retrieved by rotating the pump/circular Stokes or by rotating the pump and Stokes (see Supplement 1).

Figures 2(a)–2(d) show the result of a pure polarization modulation applied to SRS detection in a multilamellar vesicle (MLV) made of 1,2-dipalmitoyl-sn-glycero-3-phosphocholine (DPPC), a high-transition-temperature lipid known to form high-order multilayer structures [16,17]. The result of the modulation in those images is not an intensity map such as in traditional SRS, but a relative molecular order image, as a result of a response to polarization, in CH-oriented regions of the sample. The measured modulation  $S_2$  and phase  $\varphi_2$  are moreover directly and simultaneously obtained from the lock-in detection without post-processing, in contrast with previous polarization-resolved CRS approaches. Importantly, those images are obtained at a pixel rate of 50  $\mu\text{s}$  from the average over five polarization periods, which represents a significant increase in speed.

The obtained  $S_2$  image is highly contrasted [Fig. 2(a)], revealing the outside ring of the MLV spherical shape where molecular bonds are oriented over an isotropic background, where no polarization dependence is expected. This structural contrast

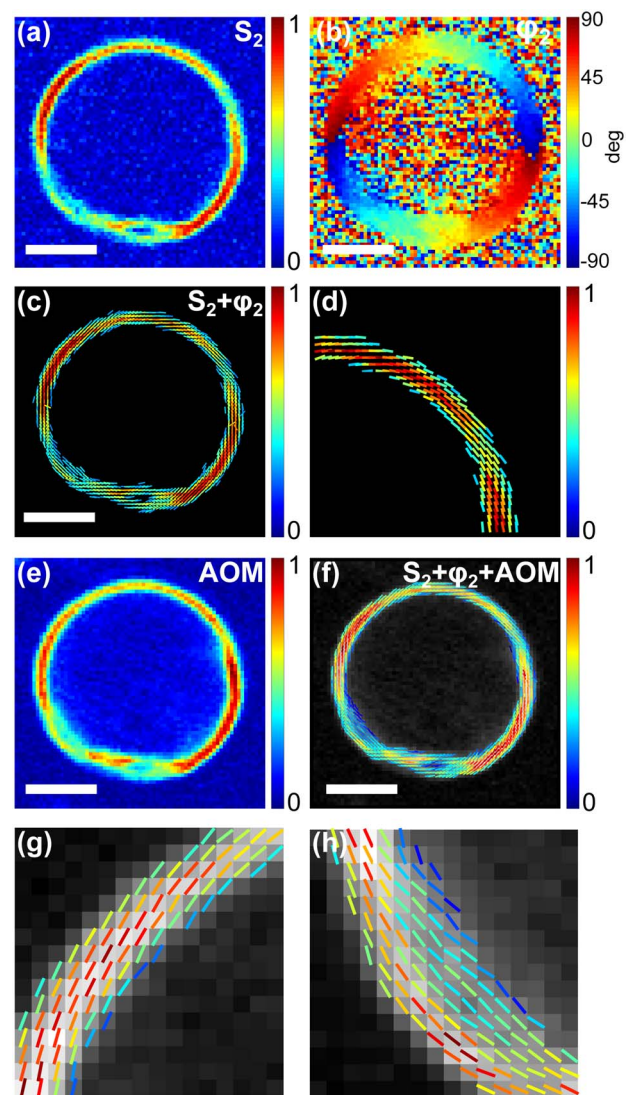


**Fig. 2.** Fast-polarization-resolved SRS in a DPPC MLV, under different modulation conditions. [(a)–(d)] Pure EOM modulation (100 kHz). (a)  $S_2$  amplitude from lock-in amplifier. (b)  $\varphi_2$  from lock-in amplifier phase. (c) Composite image showing  $\varphi_2$  as a stick, colored with  $S_2$  for each measured pixel for which  $S_2$  is greater than 4 times the mean  $S_2$  background. (d) Zoomed in view of image (c). [(e)–(h)] EOM (100 kHz) and AOM (2 MHz) double modulation. (e) SRS amplitude from lock-in amplifier at 2 MHz. (f) Composite image showing  $(S_2, \varphi_2)$  as colored sticks and the AOM amplitude as a background. (g) Zoomed in view of the top left corner of image (f). (h) Zoomed in view of the bottom left corner of image (f). In both experiments, the powers of the pump and Stokes beams are, respectively, 8 mW and 6.5 mW at the sample plane, and the image (pixel dwell time: 50  $\mu\text{s}$ ) is generated in 1 s. All  $S_2$  values are normalized with respect to the maximum in the image. Scale bars: 6  $\mu\text{m}$ . Pixel size: 300 nm.

capability is very similar to that found by symmetry filtering using circular polarizations, as presented recently [27]. Here, however, the averaged orientation  $\varphi_2$  can be additionally obtained from the phase of the SRS modulated signal [Fig. 2(b)], information, which is not accessible by symmetry filtering. Figures 2(c)–2(d) show a combined representation of amplitude and phase per image pixel, using sticks oriented with  $\varphi_2$  and colored with  $S_2$ . This representation provides information on both the local molecular order

within a given pixel and orientation persistence over several pixels. Here the measured CH molecular bonds can be seen to follow the membrane contour homogeneously [Fig. 2(d)], as expected from their direction being perpendicular to the lipid chains in tightly packed lipid multilayers [Fig. 1(c)].

At this stage, the image produced is the signature of strong molecular organization and permits visualizing relative variations at a pixel rate of 50  $\mu\text{s}$ . However, it does not provide an absolute read-out of molecular order, for which normalization by the total measured intensity (e.g., DC amplitude of the signal) per pixel is required. To provide such capability, we implemented simultaneous amplitude (AOM) and polarization (EOM) modulations of the pump beam at different frequencies [see Supplement 1, Fig. S1, and Fig. 1(e)]. Figures 2(e)–2(h) show the result of such double-modulation detection on the same MLV as in Figs. 2(a)–2(d). The AOM+EOM image produced [Fig. 2(f)] shows that using both modes simultaneously reveals very similar  $S_2$  and  $\varphi_2$  maps as compared to pure EOM [Fig. 2(c)], which emphasizes the possibility to use both modalities in an equivalent way without any compromise in signal-to-noise conditions (see Supplement 1, Fig. S4). Comparing the two modes, the SRS intensity (AOM image) shows a low signal where the polarization modulation (EOM image) was relatively lower in the sample, meaning that the absolute molecular order is likely to be rather homogeneous in this sample. New features are also visible at the border of the MLV using the intensity image [Fig. 2(h)]. Here, for instance, the local CH bond orientations,  $\varphi_2$ , are seen to deviate from the membrane contour direction in regions lower in lipid density (e.g., low SRS intensity), most probably as a result of a higher mesoscopic (pixel-size) disorder in those regions.

### 3. FAST QUANTITATIVE MOLECULAR ORDER IMAGING

In order to evaluate the potential of fast-polarization modulation for quantitative dynamic determination of molecular order, we compared the result obtained from regular-polarization SRS to that from fast-polarization SRS on the same DPPC MLV sample (Fig. 3). Regular-polarization SRS was generated by a discrete variation (typically 5° step) of the incident pump and Stokes linear polarizations, deducing amplitude and phase components ( $S_2, \varphi_2$ ) from the Fourier series decomposition of the signal recorded at each pixel of the produced image stack (see Supplement 1). This analysis is performed at the post-processing level and, thus, permits normalizing the amplitude coefficient to the total intensity per pixel, obtaining normalized coefficients  $S_{2n}$ , which can be directly interpreted as absolute molecular order values [17] [Fig. 3(a)]:

$$S_{2n} = S_2/a_0. \quad (2)$$

In the case of the fast-polarization modulation [Fig. 3(b)], this normalization procedure was obtained from the amplitude recorded via lock-in detection at the AOM modulation frequency. The  $S_{2n}$  values obtained by this procedure and their spatial dependence over the MLV contour are very similar to those obtained by regular-polarization SRS, the slight variations observed being attributed to differences in the integration times required for the two measurements. Overall, the molecular order values obtained from fast-polarization normalized SRS are also very close

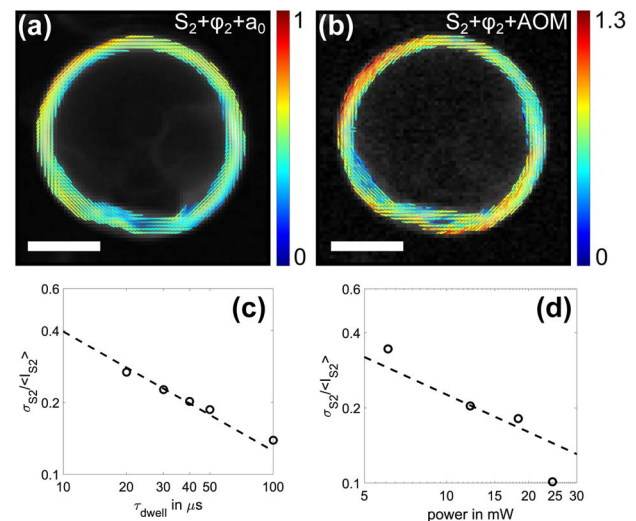


**Fig. 3.** (a) Regular-polarization SRS on a DPPC MLV, using step angles of 5° (acquisition time 112s). Absolute ( $S_{2n}, \varphi_2$ ) values are represented as colored sticks and  $a_0$  as gray-scaled background (stick directions follow similar behavior as in Fig. 2). (b) Fast-polarization SRS on the same MLV (acquisition time 1 s). Scale bars: 6  $\mu\text{m}$ . For both measurements, the powers of the pump and Stokes beams are, respectively, 8 mW and 6.5 mW at the sample plane and the pixel dwell time is 50  $\mu\text{s}$ . (c) Dependence of the standard deviation of  $S_2$ , over the MLV contour, normalized by its mean value, on the dwell time per pixel. (d) Same parameter as in panel (c), versus the total incident power. The dashed lines are an inverse square root fit of the measured data.

to those reported previously using regular-polarization SRS on DPPC MLVs [23].

Remarkably, the fast-polarization SRS image in Fig. 3(b) has been obtained in 1 s, which is two orders of magnitude faster compared with the regular-SRS image in Fig. 3(a) using the same incident powers, number of pixels, and dwell time per pixel. To assess the sensitivity of the method to the image acquisition speed, we measured the relative noise obtained on  $S_2$  for different conditions of acquisition time and incident powers. Decreasing the dwell time and power obviously increases noise, leading to higher  $S_2$  standard deviations measured over a MLV contour [Figs. 3(c) and 3(d)]. Even though the dependence found is very similar to an inverse square root law, the detection does not reach the shot noise limit since additional electronic and laser noise contributions appear at 100 kHz. Nevertheless, in the present experiment, the measured noise is seen to fall down close to shot noise levels above a modulation frequency of 600 kHz, which is, in principle, reachable for polarization modulation (see Supplement 1, Fig. S4).

These measured parameters allow quantifying the framework for which sufficient sensitivities can be attained: typically, using a dwell time below five EOM modulation periods (here 50  $\mu\text{s}$ ) is affordable but at the cost of loss of precision. Increasing the EOM modulation frequency would therefore give access, in principle, to higher acquisition rates, with more favorable noise rejection in the lock-in amplification. In addition, under the experimental parameters used here, a reduction of the pixel numbers would give access to millisecond time scales in molecular order modifications. This emphasizes the capabilities of the technique to access sub-second time dynamics.



#### 4. FAST IMAGING OF LIPID STRUCTURAL DYNAMICS

In the frequency conditions used here, sub-second time-scale molecular order imaging can be obtained on DPPC MLVs. Double EOM–AOM modulation in SRS shows that single MLVs could be observed over minutes without strong alterations of their lipid order properties [Figs. 4(a) and 4(b)]. MLVs are overall remarkably robust under prolonged illumination (see also Supplement 1, Fig. S5, and Visualization 2). Note that a prolonged focused illumination at high power could not affect the measured molecular order, probably because of the fluid nature of lipids, which tend to redistribute spatially in case of local perturbations.

This phenomenon could also be recorded in fast-polarization CARS with similar sensitivity as for SRS [28] [Figs. 4(c) and 4(d)]. Indeed, even though lock-in amplification is dedicated to the detection of a low modulation over a large background, it can considerably improve signal-to-noise ratios in CARS imaging, in particular, in the use of fast scanning capabilities as shown previously for SHG [29]. In the present case, the EOM polarization modulation provides a source for CARS signal modulation, which is quantitatively very similar to the one obtained in SRS (see Supplement 1, Fig. S6).

Despite their robustness, occasional local alteration of molecular order in MLVs could be observed at the time scale accessible in this experiment, which is typically from 0.25 s to 1 s per image. MLVs could indeed detach from the sample surface, inducing motion [Figs. 4(c) and 4(d)] or shape change (see Supplement 1, Fig. S7, and Visualization 4). Local changes manifest mostly in the mean orientation  $\varphi_2$  of the lipid distribution, signature of major modifications of their mesoscopic-scale organization,

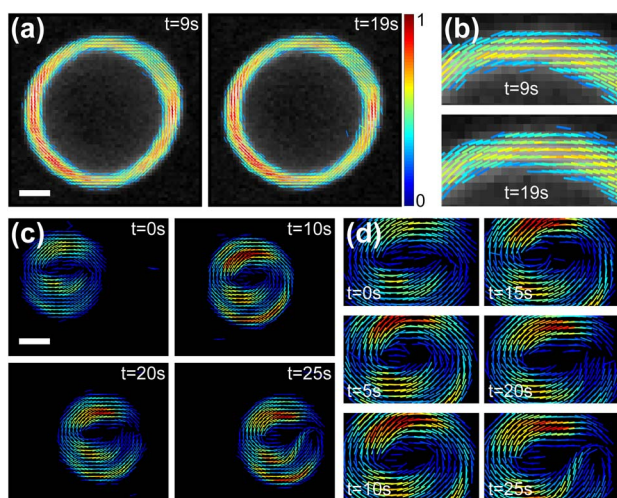


**Fig. 4.** Fast-polarization dynamics of lipid order in DPPC MLVs. All  $S_2$  values are normalized to their maximum within a time sequence. (a) SRS image of a MLV taken at different times of the observation sequence, shown as a composite image ( $S_2, \varphi_2$ ) as colored sticks, using the AOM amplitude as a (gray) background. Scale bar: 2  $\mu\text{m}$ . Pixel size: 200 nm. Pixel dwell time: 50  $\mu\text{s}$ . (see Visualization 1). (b) Zoom on the upper part of the MLV contour showing no change of lipid order during the measurement over tens of seconds. (c) CARS image sequence, taken in similar conditions, on a MLV moving over the sample surface. Scale bar: 3  $\mu\text{m}$ . Pixel size: 300 nm. Pixel dwell time: 50  $\mu\text{s}$ . (see Visualization 3). (d) Zoom on the MLV showing loss of order and reconfiguration of membrane mesoscopic geometry.

together with a local loss of order. The modifications observed in Fig. 4(d) are in particular attributed to a local membrane disruption, followed by its spontaneous reformation. Such example emphasizes the capabilities of fast-polarization vibrational imaging, which can reveal the sub-second time scale dynamics of the lipid membrane ultrastructure. In particular, it was possible here to visualize local modifications during the time course of the MLV displacement, which was not accessible using the minute-time-scale regular polarization experiments.

At the cell level, lipids are of various nature, organized in a bilayer and in interaction with proteins constantly undergoing complex dynamics. Despite the much lower signal expected [30], we were able to observe second-time-scale dynamics in thin lipid membranes down to the cell plasma membrane. Figure 5(a) depicts a typical result obtained from fast-polarization SRS on a thin DPPC MLV. The images obtained clearly show noisier  $S_2$  values than those in thick MLVs, due to the expected lower lipid content in the focal volume; however, they still clearly depict quantitative information, here, for example, high order on the border of the MLV and less ordered membranes in an inner smaller vesicle. Despite the lower level of the signal, the mean and standard deviation values obtained over the large MLV were seen to be stable over time [Fig. 5(a)].

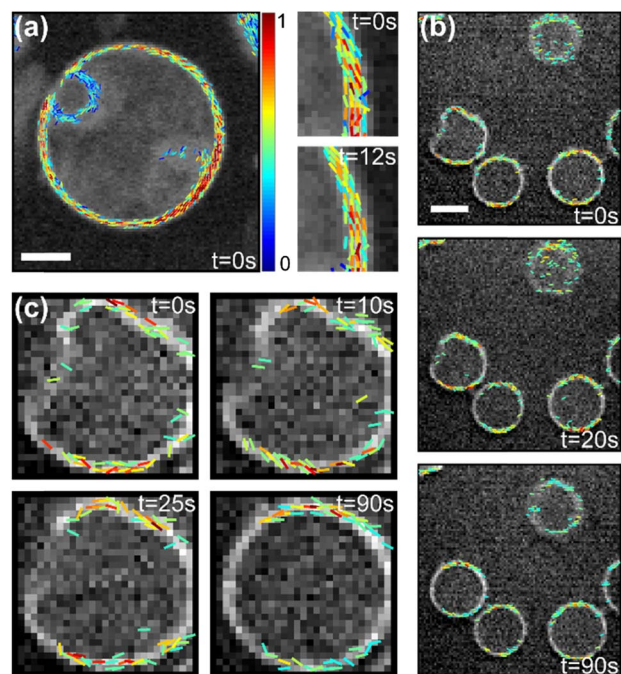


**Fig. 5.** Fast-polarization dynamics of lipid order in thin lipid membranes. All  $S_2$  values are normalized with respect to the maximum in the image sequence. The images are made of composite ( $S_2, \varphi_2$ ) as colored sticks, using the AOM amplitude as a (gray) background. (a) SRS image of a thin DPPC MLV with zooms at two times of the recorded sequence. Scale bar: 4  $\mu\text{m}$ . Pixel size: 200 nm. Pixel dwell time: 50  $\mu\text{s}$ . Power in sample plane: 20 mW. (b) CARS image sequence in red blood cell ghosts. Each image is obtained from an average of five consecutive images to increase the signal to noise per pixel (see Visualization 5). A threshold is applied, which rejects all pixels for which the  $S_2$  signal is below 1.3 times its minimal value. This permits determining, based on simulations, a bias less on  $\varphi_2$  than  $10^\circ$ . (c) Zoom on the red blood cell membrane. Scale bars: 4  $\mu\text{m}$ . Pixel size: 200 nm. Pixel dwell time: 50  $\mu\text{s}$ . Power in sample plane: 16 mW.

The even more challenging case of single lipid bilayer is depicted in Figs. 5(b) and 5(c). Red blood cells modified by osmotic treatment (see Supplement 1) could be imaged and followed for minutes under fast-polarization CARS imaging, showing membrane morphology dynamics that reflect fluctuations at various scales (see Visualization 5). However, a clear limit of such a sample is its  $S_2$  signal-to-noise conditions, which is a few orders of magnitude below that obtained in MLVs. This decrease is essentially due to the lower lipid content measured, a MLV containing typically 50–100 bilayers in the focal volume [16]. It also reflects a lower degree of lipid order due to the presence of different lipid types, proteins, and local membrane folding [31–34]; normalized  $S_{2n}$  values are indeed about five times less than those observed in MLVs. The lower  $S_2$  signal obtained in red blood cells inherently leads to a higher sensitivity to polarization distortions, in particular, the even slight di-attenuation that was measured between the  $s$  and  $p$  components of the incident pump polarization (see Supplement 1, Figs. S2 and S3). Numerical models (see Supplement 1, Fig. S8) show that this di-attenuation leads to a bias in the determination of both  $S_2$  and  $\varphi_2$ , in particular, at  $\varphi_2 \sim 90^\circ$  with an underestimation of  $S_2$  (see Supplement 1, Fig. S9, and Visualization 6). Figures 5(b) and 5(c), therefore, depicts only ( $S_2, \varphi_2$ ) values for which the confidence range on  $\varphi_2$  is within a margin of  $10^\circ$ , adapting a threshold on  $S_2$  based on simulations and measured values. Note that this effect, associated to conditions of extreme low signal to noise, is not visible in the MLV measurements described above, which resemble more general conditions used for CARS/SRS imaging. Different strategies can be used to overcome bias in parameter retrieval under such conditions, by either correcting for polarization distortions in the optical setup using compensation optics or by post-processing correction [34].

## 5. DISCUSSION AND CONCLUSIONS

Fast-polarization CRS imaging is demonstrated with the possibility to monitor second to sub-second time scale dynamics in lipid samples, down to single-cell membranes. This method allows access to local order ( $S_2$ ) and mean orientation ( $\varphi_2$ ) information simultaneously at a rate two orders of magnitude faster than that in regular-polarization CRS modalities; the rate could be made faster by the use of higher EOM modulation frequencies. The parameters of both orders ( $S_2, \varphi_2$ ) provide complementary information. The local order  $S_2$  is a picture of the angular constraint experienced by the molecular bonds within the microscope focal spot, which quantifies molecular-scale disorder behavior occurring at the sub-diffraction scale. In contrast, the mean orientation  $\varphi_2$  of the bond distribution is rather a mesoscopic-scale information occurring at the pixel scale, typically of 100 nm–300 nm size. It permits, for instance, quantifying the persistence or, on the contrary, the randomness of local orientations over distances from several hundreds of nanometers to micrometric scales, with a time scale of seconds. Both information are not present in conventional CRS, opening the possibility to access structural information on lipids in single cells and tissues. The technique has, in particular, capabilities to relate structural lipid packing dynamics to lipid phase formation and protein redistributions at fast time scales, but also to their regulation dynamics, which has been imaged recently by CRS in lipid droplets in cells [35] and tissues [2]. Higher refinement in lipid order monitoring can be brought by measuring both  $S_2$  and its fourth-order counterpart  $S_4$ , which

provides information on the shape of the measured distribution. This can be made possible by tuning both pump and Stokes polarizations [17], using two synchronized Pockels cells that address both excitation wavelengths independently.

Applications in biomedical optics are also promising, following the growing interest in monitoring lipid organization in myelin, a possible marker for early detection of neurodegenerative diseases [20–22]. Adapting polarized structural imaging for *in vivo* imaging is accessible, as shown already by *in vivo* CARS imaging [36]; however, it would necessitate the implementation of epi-detection modalities. To explore this direction, we have tested the fast-polarization CARS methodology in the epi mode, demonstrating very similar results as in forward detection (see Supplement 1, Fig. S10, and Visualization 7). Epi mode fast-polarization SRS would require the use of a beamsplitter at the expense of a loss of signal, which, however, would not be a limit in the observation of dense lipid structures such as myelin [23].

At last, the method opens prospective possibilities in the use of broadband spectral SRS/CARS detection schemes, which allow monitoring specific chemical species in cells, more specifically, around the lipid band region where different lipid types can be discriminated [3,4]. Raman spectra of individual blood cells are known, for instance, to show spectral features characteristic to tumor cells [37]. Polarization modulation between two polarization states has been used recently in combination with amplitude modulation for optimizing spectral focusing in SRS microscopy, essentially by eliminating cross-phase modulation in isotropic samples [38]. This scheme could be advantageously combined with the present method in non-isotropic samples such as those studied here, in order to increase the robustness of spectral measurement in broadband SRS configurations where polarization sensitivity is required. Note that hyperspectral analyses require disentangling the content of complex molecular bond mixtures. In this context, the modulation signals measured in this work can be interpreted into orientation distribution of vibrational bonds provided their symmetry is known, using microscopic to macroscopic frame transformations as detailed in [15,39].

Overall, the proposed method, applied as a new structural vibrational imaging scheme, is able to address the increasing demand for chemically specific dynamics imaging.

**Funding.** Agence Nationale de la Recherche (ANR) (ANR-10-INBS-04-01, ANR-11-INBS-0006, ANR-15-CE19-0018-01).

\*These authors contributed equally to this work.

See Supplement 1 for supporting content.

## REFERENCES

1. A. Zumbusch, G. R. Holtom, and X. S. Xie, "Three-dimensional vibrational imaging by coherent anti-Stokes Raman scattering," *Phys. Rev. Lett.* **82**, 4142–4145 (1999).
2. C. W. Freudiger, W. Min, B. G. Saar, S. Lu, G. R. Holtom, C. He, J. C. Tsai, J. X. Kang, and X. S. Xie, "Label-free biomedical imaging with high sensitivity by stimulated Raman scattering microscopy," *Science* **322**, 1857–1861 (2008).
3. C. H. Camp, Jr. and M. T. Cicerone, "Chemically sensitive bioimaging with coherent Raman scattering," *Nat. Photonics* **9**, 295–305 (2015).
4. J.-X. Cheng and X. S. Xie, "Vibrational spectroscopic imaging of living systems: an emerging platform for biology and medicine," *Science* **350**, aaa8870 (2015).

5. C. L. Evans, E. O. Potma, M. Puoris'haag, D. Cote, C. P. Lin, and X. S. Xie, "Chemical imaging of tissue *in vivo* with video-rate coherent anti-Stokes Raman scattering microscopy," *Proc. Natl. Acad. Sci. USA* **102**, 16807–16812 (2005).
6. B. G. Saar, C. W. Freudiger, J. Reichman, C. M. Stanley, G. R. Holtom, and X. S. Xie, "Video-rate molecular imaging *in vivo* with stimulated Raman scattering," *Science* **330**, 1368–1370 (2010).
7. D. Fu, G. Holtom, C. Freudiger, X. Zhang, and X. S. Xie, "Hyperspectral imaging with stimulated Raman scattering by chirped femtosecond lasers," *J. Phys. Chem. B* **117**, 4634–4640 (2013).
8. C.-S. Liao, M. N. Slipchenko, P. Wang, J. Li, S.-Y. Lee, R. A. Oglesbee, and J.-X. Cheng, "Microsecond scale vibrational spectroscopic imaging by multiplex stimulated Raman scattering microscopy," *Light Sci. Appl.* **4**, e265 (2015).
9. C.-S. Liao, K.-C. Huang, W. Hong, A. J. Chen, C. Karanja, P. Wang, G. Eakins, and J.-X. Cheng, "Stimulated Raman spectroscopic imaging by microsecond delay-line tuning," *Optica* **3**, 1377–1380 (2016).
10. S. Brasselet, "Polarization-resolved nonlinear microscopy: application to structural molecular and biological imaging," *Adv. Opt. Photon.* **3**, 205–271 (2011).
11. J.-X. Cheng, S. Pautot, D. A. Weitz, and X. S. Xie, "Ordering of water molecules between phospholipid bilayers visualized by coherent anti-Stokes Raman scattering microscopy," *Proc. Natl. Acad. Sci. USA* **100**, 9826–9830 (2011).
12. A. V. Kachynski, A. N. Kuzmin, P. N. Prasad, and I. I. Smalyukh, "Coherent anti-Stokes Raman scattering polarized microscopy of three-dimensional director structures in liquid crystals," *Appl. Phys. Lett.* **91**, 151905 (2007).
13. B. G. Saar, H.-S. Park, X. S. Xie, and O. D. Lavrentovich, "Three-dimensional imaging of chemical bond orientation in liquid crystals by coherent anti-Stokes Raman scattering microscopy," *Opt. Express* **15**, 13585–13596 (2007).
14. M. Zimmerley, R. Younger, T. Valenton, D. C. Oertel, J. L. Ward, and E. O. Potma, "Molecular orientation in dry and hydrated cellulose fibers: a coherent anti-Stokes Raman scattering microscopy study," *J. Phys. Chem. B* **114**, 10200–10208 (2010).
15. F. Munhoz, H. Rigneault, and S. Brasselet, "High order symmetry structural properties of vibrational resonances using multiple-field polarization coherent anti-Stokes Raman spectroscopy microscopy," *Phys. Rev. Lett.* **105**, 123903 (2010).
16. G. W. H. Wurpel, H. A. Rinia, and M. Muller, "Imaging orientational order and lipid density in multilamellar vesicles with multiplex CARS microscopy," *J. Microsc.* **218**, 37–45 (2005).
17. F.-Z. Bioud, P. Gasecka, P. Ferrand, H. Rigneault, J. Duboisset, and S. Brasselet, "Structure of molecular packing probed by polarization-resolved nonlinear four-wave mixing and coherent anti-Stokes Raman scattering microscopy," *Phys. Rev. A* **89**, 013836 (2014).
18. Y. Fu, T. B. Huff, H.-W. Wang, J.-X. Cheng, and H. Wang, "Ex vivo and *in vivo* imaging of myelin fibers in mouse brain by coherent anti-Stokes Raman scattering microscopy," *Opt. Express* **16**, 19396–19409 (2008).
19. G. de Vito, A. Bifone, and V. Piazza, "Rotating-polarization CARS microscopy: combining chemical and molecular orientation sensitivity," *Opt. Express* **20**, 29369–29377 (2012).
20. G. de Vito, V. Cappello, I. Tonazzini, M. Cecchini, and V. Piazza, "RP-CARS reveals molecular spatial order anomalies in myelin of an animal model of Krabbe disease," *J. Biophoton.* **10**, 385–393 (2017).
21. P. Gasecka, A. Jaouen, F.-Z. Bioud, H. B. de Aguiar, J. Duboisset, P. Ferrand, H. Rigneault, N. Balla, F. Debarbieux, and S. Brasselet, "Lipid order degradation in autoimmune demyelination probed by polarization resolved coherent Raman microscopy," *bioRxiv* (2017), doi: 10.1101/105965.
22. R. Turcotte, D. J. Rutledge, E. Bélanger, D. Dill, W. B. Macklin, and D. C. Côté, "Intravital assessment of myelin molecular order with polarimetric multiphoton microscopy," *Sci. Rep.* **6**, 31685 (2016).
23. J. Duboisset, P. Berto, P. Gasecka, F.-Z. Bioud, P. Ferrand, H. Rigneault, and S. Brasselet, "Molecular orientational order probed by coherent anti-Stokes Raman scattering (CARS) and stimulated Raman scattering (SRS) microscopy: a spectral comparative study," *J. Phys. Chem. B* **119**, 3242–3249 (2015).
24. M. Samim, D. Sandkuijl, I. Tretyakov, R. Cisek, and V. Barzda, "Differential polarization nonlinear optical microscopy with adaptive optics controlled multiplexed beams," *Int. J. Mol. Sci.* **14**, 18520–18534 (2013).
25. P. Stoller, B.-M. Kim, A. M. Rubenchik, K. M. Reiser, and L. B. Da Silva, "Polarization-dependent optical second-harmonic imaging of a rat-tail tendon," *J. Biomed. Opt.* **7**, 205–214 (2002).
26. J. I. Dadap, J. Shan, A. S. Weling, J. A. Misewich, and T. F. Heinz, "Homodyne detection of second-harmonic generation as a probe of electric fields," *Appl. Phys. B* **68**, 333–341 (1999).
27. C. Cleff, A. Gasecka, P. Ferrand, H. Rigneault, S. Brasselet, and J. Duboisset, "Direct imaging of molecular symmetry by coherent anti-Stokes Raman scattering," *Nat. Commun.* **7**, 11562 (2016).
28. Y. Ozeki, F. Dake, S. Kajiyama, K. Fukui, and K. Itoh, "Analysis and experimental assessment of the sensitivity of stimulated Raman scattering microscopy," *Opt. Express* **17**, 3651–3658 (2009).
29. E. L. DeWalt, S. Z. Sullivan, P. D. Schmitt, R. D. Muir, and G. J. Simpson, "Polarization-modulated second harmonic generation ellipsometric microscopy at video rate," *Anal. Chem.* **86**, 8448–8456 (2014).
30. E. O. Potma and X. S. Xie, "Detection of single lipid bilayers with coherent anti-Stokes Raman scattering (CARS) microscopy," *J. Raman Spectrosc.* **34**, 642–650 (2003).
31. D. A. Cheresh, J. Leng, and R. L. Klemke, "Regulation of cell contraction and membrane ruffling by distinct signals in migratory cells," *J. Cell Biol.* **146**, 1107–1116 (1999).
32. A. Anantharam, B. Onoa, R. H. Edwards, R. W. Holz, and D. Axelrod, "Localized topological changes of the plasma membrane upon exocytosis visualized by polarized TIRFM," *J. Cell Biol.* **188**, 415–428 (2010).
33. R. K. P. Benninger, B. Vanherberghen, S. Young, S. B. Taner, F. J. Culley, T. Schnyder, M. A. A. Neil, D. Wüstner, P. M. W. French, D. M. Davis, and B. Önfelt, "Live cell linear dichroism imaging reveals extensive membrane ruffling within the docking structure of natural killer cell immune synapses," *Biophys. J.* **96**, L13–L15 (2009).
34. A. Kress, X. Wang, H. Ranchon, J. Savatier, H. Rigneault, P. Ferrand, and S. Brasselet, "Mapping the local organization of cell membranes using excitation-polarization-resolved confocal fluorescence microscopy," *Biophys. J.* **105**, 127–136 (2013).
35. X. Nan, "Vibrational imaging of lipid droplets in live fibroblast cells with coherent anti-Stokes Raman scattering microscopy," *J. Lipid Res.* **44**, 2202–2208 (2003).
36. E. Bélanger, F. P. Henry, R. Vallée, M. A. Randolph, I. E. Kochevar, J. M. Winograd, C. P. Lin, and D. Côté, "In vivo evaluation of demyelination and remyelination in a nerve crush injury model," *Biomed. Opt. Express* **2**, 2698–2708 (2011).
37. S. Dochow, C. Beleites, T. Henkel, G. Mayer, J. Albert, J. Clement, C. Krafft, and J. Popp, "Quartz microfluidic chip for tumour cell identification by Raman spectroscopy in combination with optical traps," *Anal. Bioanal. Chem.* **405**, 2743–2746 (2013).
38. M. Andreana, M.-A. Houle, D. J. Moffatt, A. Ridsdale, E. Buettner, F. Légaré, and A. Stolow, "Amplitude and polarization modulated hyperspectral stimulated Raman scattering microscopy," *Opt. Express* **23**, 28119–28131 (2015).
39. R. P. Davis, A. J. Moad, G. S. Goeken, R. D. Wampler, and G. J. Simpson, "Selection rules and symmetry relations for four-wave mixing measurements of uniaxial assemblies," *J. Phys. Chem. B* **112**, 5834–5848 (2008).